Weierstraß–Institut
für Angewandte Analysis und Stochastik

im Forschungsverbund Berlin e.V.

Phase transitions of shape memory alloys in soft and hard loading devices

Michael Schwarz

submitted: 28th June 1996

Weierstrass Institute
for Applied Analysis
and Stochastics
Mohrenstraße 39
D – 10117 Berlin
Germany

Preprint No. 251
Berlin 1996

1991 Mathematics Subject Classification. 34A09, 34A50, 82D25.
Key words and phrases. Phase transitions, shape memory alloys, rate laws.

Edited by
Weierstraß–Institut für Angewandte Analysis und Stochastik (WIAS)
Mohrenstraße 39
D — 10117 Berlin
Germany

Fax: + 49 30 2044975
e–mail (X.400): c=de;a=d400-gw;p=WIAS-BERLIN;s=preprint
e–mail (Internet): preprint@wias-berlin.de

Abstract

Shape memory alloys exhibit a complex load deformation temperature behaviour (especially e.g. hysteresis and "inner" loops) which is due to the occurence of a first order phase transition. By load deformation diagrams the so-called shape memory effect can be made visible. We study a model of I. Müller et al. [1], based on statistical mechanics, which is applicable to biaxial loading of polycrystalline bodies and incorporates the rotational part of a deformation. Recently, I. Müller et al. [3] have proposed a second model incorporating the coherence energy for solid phase mixtures. For two principle variants of experiments (soft and hard loading devices) we present numerical simulations of load deformation curves for either of the two models. Comparing these with experimental results of so-called "inner loops" in a hystersis the second model shows its superiority.

1 Introduction

In the last years *Shape Memory Alloys* like *NiTi, CuAlNi, AuCnZn* or *CuAlZn* have gained much attraction from the point of view of applications. The importance of these smart materials is a result of the *Shape Memory Effect.* This effect is produced by the hysteretic behaviour of the material. Hysteresis is the result of a phase transitition between phases in the alloy.

1.1 The Shape Memory Effect

At first we describe the *Shape Memory Effect*, which may be defined as the recovery of the original shape of a specimen upon heating after a (quasi-) plastic deformation. Consider in fig. 1 the schematic picture of a straight wire, which is bent into a spiral at *low temperature*. After heating it recovers its straight shape and retains it even after *cooling down* to the initial temperature. The recoverable strain is typically about 5-8% in a temperature range from about $30 - 50°$ C. The so-called *Shape Memory Effect* may be read from load deformation diagrams, which will be simulated . The impact to applications in industry and medicine is obvious. However, the case of a two-way *Shape Memory Effect* is not considered here. In that case, there are only two possible states of deformation for the material, realizing a mechanical switch.

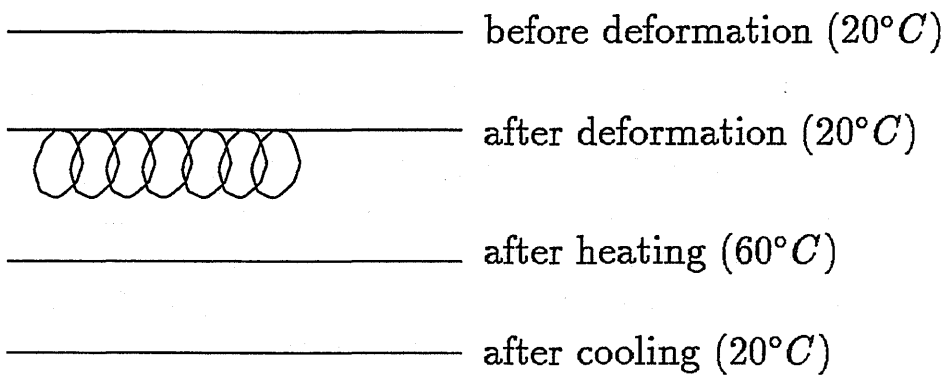

Fig. 1: The shape memory effect (cf. fig. 1.1 in [3])

1.2 Load Deformation Diagrams

To visualize the *Shape Memory Effect* we consider some schematic load-deformation diagrams for different temperatures $T_1 < T_2 < T_3 < T_4$ in fig. 2.

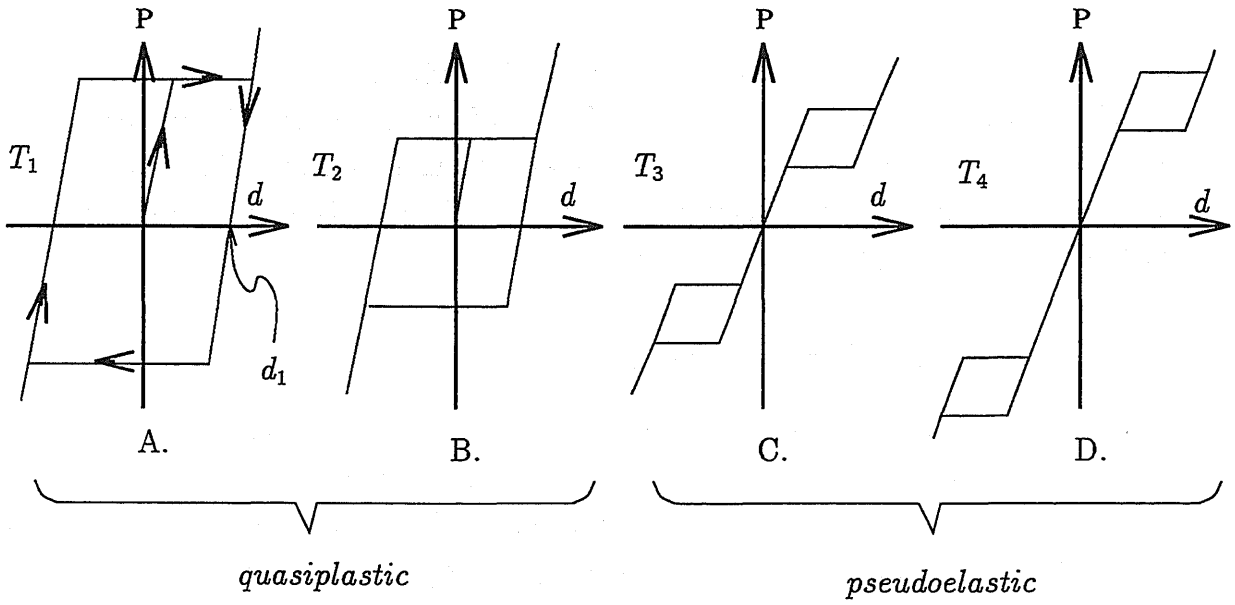

Fig. 2: Load-deformation diagrams: Quasi-plasticity (A,B) and pseudo-elasticity (C,D) (cf. fig. 1.2 in [3])

In the so-called quasiplastic temperature range (subfig. A–B) we start a tensile loading $P > 0$ from the origin (d=0, P=0). Following the *virginal curve* with an elastic deformation path, there is a yield limit (after that, there is also an elastic branch) and upon unloading, we reach the point $(0, d_1)$, i.e. a residual deformation. Upon compressively loading ($P < 0$) subfigure A shows in an analogous manner a *hysteresis loop*, which is followed by a process with alternatively tensile and compressive loading. Subfigure B shows the same qualitative behaviour for a higher

temperature $T_2 > T_1$ with a decreased yield limit. Because of the yield limit this temperature range is called quasiplastic[1] or ferroelastic. For higher temperatures, in the *pseudoelastic range*, the picture changes significantly, because there remains an elastic line through the origin and now, there are two (smaller) hysteresis loops in the first resp. third quadrant. The shape memory effect may be read from fig. 2A–C. Having reached the point $(0, d_1)$ upon loading at temperature T_1 we heat the body and see in fig. 2.C that this point is not a valid, i.e. stable state, so that the body will return to the origin assuming the shape before the deformation. So the material "remembers" its orignal shape and even in cooling down from T_3 to T_1 this state remains valid.

1.3 Soft and Hard Loading Devices

In a uniaxial tensile experiment with a specimen made of *Shape Memory Alloy* (cf. fig. 3) one can distinguish *soft-* and *hard loading devices*. In a soft loading device the load on the specimen (cf. fig. 3) is prescribed and the resulting deformation is measured, and for a hard loading device the situation is vice versa (deformation-driven experiments).

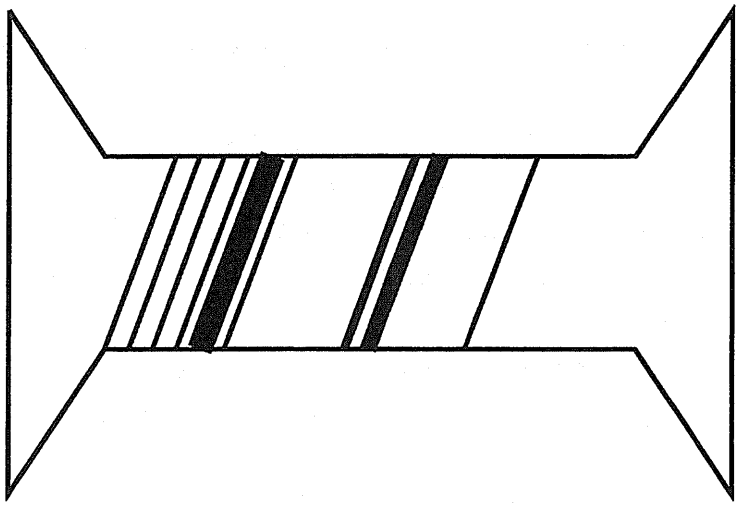

Fig. 3: A typical specimen for the *soft* and *hard loading devices* made of a shape memory alloy (cf. fig. 1.3 in [3]). The total length is here about 5 cm, the width of the narrow part 0.8 cm and the thickness about 0.15 cm. The lines mark a different phase.

In a series of papers, Falk ([4] and the references therein) has proposed a model for shape memory alloys by defining a free energy of Landau-Devonshire-Ginzburg type. Sprekels et al (cf. [5] and the references therein) have shown existence and

[1]Unlike plasticity it is possible to load elastically after the yield load has been reached.

uniqueness for the mathematical model and proposed a numerical scheme ([6]). Klein ([7]) showed stability and uniqueness of this scheme and carried out numerical simulations for a soft loading device. In his dissertation, Bubner ([8], [?]) modified the Falk model for the case of a hard loading device and presented numerical calculations for that in the low temperature range. It turns out that for the latter case there are "inner loops" in the "greater" hysteresis (cf. fig. 2.A) We will see this in the last section, too. However, these simulations have been down only in one dimension (for the simulation of a wire).
Metallurgists have discovered that in the described experiments phase transitions take place between *austenite*, a highly symmetric lattice structure and *martensite*, which is less symmetric, or between variants of martensites (*"twinning"*). Roughly spoken, martensite is a sheared version of austenite with twenty-four possible variants in three dimensions. The temperature dependence of a load deformation diagram is a result from the fact that austenite is a high-temperature phase and martensite prevails at low temperatures. In fig. 3 the nucleation of phases resp. the phase transition is made visible by black lines. A reasonable model must incorporate the energy balance in order to take the effect of latent heat at a transition into account.

2 Two Models from Statistical Mechanics

The starting point for both models is a *lattice particle* (a small piece of the metallic lattice); so the models are of a mesoscopic type. Considering only plane strain, there are two martensitic variants, which may be identified as sheared version M^+ resp. M^- of austenite A. The phase of each lattice particle is defined by a (triple well) potential energy function $\phi(\triangle, \tau)$ (cf. fig. 4), where $\triangle$ is the shear length and τ is the external force, acting onto this particle. So we say that a lattice particle is in the phase M^- if $\triangle < \mu_L$ and in an analogous manner, we define the phases A and M^+.
Notice, that this potential energy has nothing in common with the global phenomenological free energy of Falk. However, Müller has shown in [3] that for reasonable assumptions such a temperature dependent, non convex free energy may be constructed from this mesoscopic model, especially from the rate laws for the phase fractions.
The particles are stacked in layers, where it is assumed that they have the same $\triangle$. Stacks with different orientation angles are grouped together to form a polycrystal. In a first-order approximation a deformation of the whole body is then assumed to be a shearing motion of the layers and a rotation.

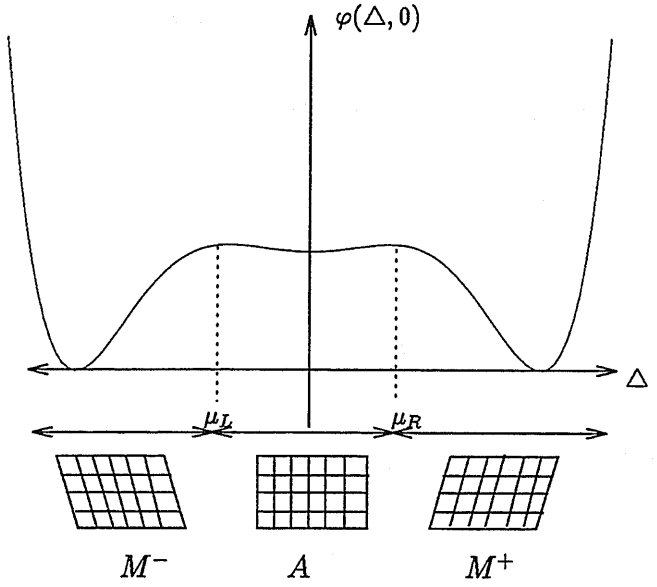

Fig. 4: Potential energy for a lattice particle (cf. fig. 1 in [1])

By statistical mechanics the model may be written as an implicit system of six integro[2] ODEs for the time-dependent variables of the model:

- volume fractions of phases $\vec{x} := (M^-, A, M^+)$,
- deformation tensor F_{ij}, $(1 \leq i, j \leq 2)$,
- angle of a layer α and
- absolute temperature T.

This results in $H(\vec{x}, \dot{\vec{x}}, T, \dot{T}, \alpha, \dot{\alpha}; F_{ij}, \dot{F_{ij}}\sigma, \dot{\sigma}, T_E) = 0$, where external temperature T_E and external stress σ (resp. the given deformation) for a soft (resp. hard) loading device are prescribed.

2.1 The Rate Laws for the first Model

Let us recall shortly the governing equations of the model [1] for a soft loading device. With $\tau := \tau_\alpha$ being the "projected" force on a layer with orientation α, the expectation value $D = D_\alpha$ for the shear length of one layer is $D = \sum_{k=1}^{3} X_k \cdot x_k$ with

$$X_k := \frac{\int_{I_k} \Delta \exp(-\varphi(\Delta, \tau)/kT) d\Delta}{\int_{I_k} \exp(-\varphi(\Delta, \tau)/kT) d\Delta}$$

[2]This originates from the modelled distribution of angles $\alpha(t)$ of each stack.

where I_1, I_2 and I_3 are the (semiinfinite) intervals $(-\infty, \mu_L), (-\mu_L, \mu_R), (\mu_\tau, \infty)$ (cf. fig. 4) and k is the Boltzmann constant[3] .
The relation of τ_α to the externally applied stress tensor σ is given by the well-known Mohr circle

$$\tau_\alpha = \frac{\sigma_{22} - \sigma_{11}}{2} \sin(2\alpha) + \sigma_{12} \cos(2\alpha).$$

The distribution of angles in a polycrystal is described by the function g:

$$\int_o^\pi g(\alpha, t) d\alpha = 1$$

.

I. Deformation Tensor The evolution of F is described by

$$\dot{F}_{ij} = \int_0^\pi g(\alpha, t) \frac{1}{h} \begin{pmatrix} -\dot{D} \sin(\alpha)\cos(\alpha) & \dot{D}\cos^2(\alpha) - \dot{\alpha} \\ -\dot{D}\sin^2(\alpha) + \dot{\alpha} & \dot{D}\sin(\alpha) + \cos(\alpha) \end{pmatrix}_{ik} F_{ik} d\alpha,$$

where h is the height of a layer, which is assumed to remain constant.

II. Phase Fractions

For each layer with orientation α, the phase fractions $\vec{x} = \vec{x_\alpha}$ evolve with

$$\dot{\vec{x}} = P_\alpha(T, \tau) \cdot \vec{x},$$

where $P = P_\alpha$ is a matrix of transition probabilities:

$$P = \begin{pmatrix} P_{11} & P_{12} & 0 \\ P_{21} & P_{22} & P_{23} \\ 0 & P_{32} & P_{33} \end{pmatrix}.$$

E.g. for the transition $M^- \to A$, we have

$$P_{11} = K\sqrt{kT} \frac{\exp(-\varphi(\mu_L, \tau)/kT)}{\int_{-\infty}^{\mu_L} \exp(-\varphi(\mu_L, \tau)/kT)}$$

with some proportionality constant K. By this, the change in, e.g., x_1 (M^-) is composed of a gain in particles, which switch over from x_2 (A), and a loss of those of M^-, which switch over to A. Note that it is impossible for particles of M^- to switch directly to M^+. First, a layer of M^- must change to austenite A and then, it can become M^+.

The introduction of matrix P models a phase transition as an activated process, because P_{ij} depends directly on the two external variables T and P_E (we are in the case of a soft loading device). As pointed out earlier, this makes it possible for Müller to construct a global non convex free energy from this model, which is the starting point for the investigations of Falk.

[3]Notice that k may appear as summation index also (and then we omit by default the range $k = 1, 2, 3$). The meaning should be clear from the context.

III. Energy Balance

For internal energy U and kinetic energy K we have

$$\frac{d(U+K)}{dt} + \int_{\partial V} q_i n_i df = \sigma_{ij} \dot{F}_{ik} {F_{kj}}^{-1} V$$

(with the usual abbreviations (ref. [1]) V being the volume and ∂V the surface of the body), which reads by using Newton's law now

$$\begin{aligned} C\dot{T} &= -w(T - T_E) + \sigma_{ij} \dot{F}_{ik} {F_{kj}}^{-1} V \\ &\quad -N \int_0^\pi g(\alpha, t) \sum_k Y_k \dot{x_k} d\alpha \\ &\quad -NfJ \int_0^\pi g(\alpha, t) \left[T \cdot S_\alpha - \sum_k X_k x_k \right] \cdot \left(\frac{\partial \tau}{\partial \alpha} \cdot \dot{\alpha} + \frac{\partial \tau}{\partial \sigma_{ij}} \cdot \dot{\sigma_{ij}} \right) d\alpha \end{aligned}$$

where N is the number of particles, and w, f, J are constants,

$$Y_k := \frac{\int_{I_K} \varphi(\triangle, \tau) \exp(-\varphi(\triangle, \tau)/kT) d\triangle}{\int_{I_K} \exp(-\varphi(\triangle, \tau)/kT) d\triangle},$$

$$\text{specific heat } C = N \int_0^\pi g(\alpha, t) R_\alpha d\alpha + \frac{\partial U}{\partial T}$$

and $S_\alpha = \frac{\partial D}{\partial T}$.

The term R_α in the expression for the specific heat is computed as follows:

$$\begin{aligned} kT^2 R_\alpha &= \sum_{i=1}^{3} \left[\frac{\left(\int_{I_i} \varphi^2(\triangle, \tau) \exp(-\varphi(\triangle, \tau)/kT) d\triangle \right) \left(\int_{I_i} \exp(-\varphi(\triangle, \tau)/kT) d\triangle \right)}{\left(\int_{I_i} \exp(-\varphi(\triangle, \tau)/kT) d\triangle \right)^2} \right. \\ &\quad \left. - \frac{\left(\int_{I_i} \varphi(\triangle, \tau) \exp(-\varphi(\triangle, \tau)/kT) d\triangle \right)^2}{\left(\int_{I_i} \exp(-\varphi(\triangle, \tau)/kT) d\triangle \right)^2} \right]. \end{aligned} \tag{1}$$

To summarize, this system of seven integro ODEs for the soft loading device allows us to calculate F_{ij}, x_k and T, the latter, to take into account the effects of latent heat (cf. Y_k).

The right hand side of the system is lineary dependent in $\dot{F}_{ij}, \dot{T}, \dot{x_k}$ and nonlinearly dependent in F_{ij}, T, x_k, σ and $\dot{\sigma}$. Because of the natural constraint $\sum_k x_k = 1$, only six equations are independent. Müller proposed to discretize the distribution of angles α in e.g. ν directions, so that the system is converted from integro ODEs to a system of $2\nu + 4$ ODEs. Notice, however, that the right hand-side then still contains semiinifinite integrals as coefficients.

2.2 Special Case

Some special assumptions have been made to fit the setting of the experiments. So the body is subject to a tensile or compressive load in one direction, where the vertical sides of the body remain vertical. For simulating experiments with unicrystals we assume a body, which contains initially only particles with a single orientation of $\frac{\pi}{4}$.
We achieve thereby the simplification of the Mohr circle to $\tau_\alpha = \tau(P(t), F_{11}, \alpha)$, where $P(t)$ is the external load (not to be confused with the matrix of transition probabilities). Furthermore, the rate laws for F_{ij} can be reduced to one rate law for $D = D_\alpha$:

$$D = K_\alpha \dot{\tau} + S_\alpha \dot{T} + \sum_k X_k \dot{x}_k, \; S_\alpha := \frac{\partial D}{\partial T}, \; K_\alpha := \frac{\partial D}{\partial \tau};$$

and there is the relation

$$F_{11} = \frac{\sqrt{2}}{\sqrt{1 + \left(1 + \frac{D}{h}\right)^2}}.$$

With $c := C/Nm$ (m the mass of a layer) the energy balance is reduced to

$$\begin{aligned} c\dot{T} &= -\frac{V}{L^2 N m} P_E(t) \frac{\dot{F}_{11}}{F_{11}^2} \\ &- \frac{W}{Nm} (T - T_E(t)) \\ &+ \sum_k Y_k \dot{x}_k \\ &+ \frac{fh}{m} \left(T \cdot S_\alpha - \sum_k X_k \dot{x}_k \right), \end{aligned}$$

where L^2 is the ground surface and V the volume of the body.

2.3 Mathematical Model

We investigate the case of section 2.2. After making the variables dimensionless and sorting the time derivatives of the solution vector on the left side, we arrive at the following system of ODE's for the soft loading device:

$$B(\vec{y}) \cdot \dot{\vec{y}} = f(\vec{y}; T_E(t), P_E(t)), \; \vec{y}(0) = \vec{y_0}, \tag{2}$$

with $\vec{y} := (\vec{x}, d, T) \in \mathbb{R}^4 \times \mathbb{R}^+, d :=$ deformation and

$$B = \begin{pmatrix} I^{3\times 3} & & \\ & 1 - P_E(t) \cdot [c_1(y) + S \cdot c_4(y)] & 0 \\ & -P_E(t) \cdot c_4(y) & 1 \end{pmatrix}. \tag{3}$$

In the right-hand side

$$f = \begin{pmatrix} P \cdot \vec{x} \\ -sW(T - T_E) + S\vec{c_6}\vec{x} + \vec{Y}P \cdot \vec{x} \\ c_5\dot{P}_E - W(T - T_E) \end{pmatrix} \tag{4}$$

there is the dimensionless matrix of transition probabilities with the structure

$$P = \begin{pmatrix} -P_{12} & P_{21} & \\ P_{12} & -(P_{21} + P_{23}) & P_{32} \\ & P_{23} & -P_{32} \end{pmatrix}. \tag{5}$$

The other coefficients of the system are similar to the one defined above, e.g.,

$$s := \frac{1}{T^2} \sum_k \frac{b_{k11} \cdot b_{k00} - b_{k01} \cdot b_{k10}}{b_{000}^2}$$

where we have defined

$$b_{klm} := \int_{I_k} \delta^l \varphi^m(\delta, P_E) \exp\left(-\frac{\varphi(\delta, P_E)}{T}\right) d\delta \tag{6}$$

and $c_1, \ldots, c_6$ are not written down for reasons of brevity.
Matrix B may be singular and therefore, we can only show local existence for the given IVP yet:

Lemma 1 *For continuous $P_E, T_E \in L^\infty[0, \infty]$ with $P_E(0) = 0$, there is a $t_1 > 0$, such that there is a unique solution to the given system of ODEs in the time intervall $[0, t_1)$.*

This is a direct consequence of the continuity of B and f, such that

$$P_E(t) \cdot [c_1(y) + S(y, P_E(t)) \cdot c_4(y)] < 1$$

and therefore B^{-1} exists in $[0, t_1)$. Having shown the existence of B^{-1}, the proof is finished by using the theorem of Picard-Lindelöf.
The special structure of the matrix of transition probabilities P shows that $\sum_k \dot{x_k} = 0$. Assuming $\sum_k x_k(0) = 1$ (which is the only solution that makes sense, since x_k are phase fractions), we arrive at $\sum_k x_k(t) = 1$ for all $t \geq 0$.
Furthermore, we can exclude that a phase fraction will become negativ, if the elements of P behave as probabilities:

Lemma 2 *For continuous* $x_i(t) \in L^\infty[0,t_1]$ *and if* $P_{ij} \geq 0$, *we have*

$$x_i(0) \in [0,1] \Rightarrow x_i(t) \in [0,1] \; \forall t \geq 0, \; i = 1,2,3.$$

Proof: It suffices to show that $x_i(t) \geq 0 \forall i$. Assume, that there is a $\tilde{t} > 0$ with $x_i(\tilde{t}) < 0$ for one particular i. From continuity there must be a t^* with $t^* := \min_{t \geq 0} \{x_i(t) = 0, i \in \{1,2,$
FIRST CASE: Let $x_1(t^*) = x_2(t^*) = 0$, then $x_3(t^*) = 1$. Therefore

$$\begin{cases} \dot{x_1}(t^*) = 0, \\ \dot{x_2}(t^*) = P_{32} \geq 0, \\ \dot{x_3}(t^*) = -P_{32} \leq 0. \end{cases}$$

So $\dot{x_2}(t^*) = 0$; otherwise $\dot{x_2}(t^*) > 0$, i.e. $\exists t < t^*$ with $x_2(t) = 0$, which contradicts the minimality of t^*. We conclude that $P_{32} = 0 \Rightarrow \dot{x_3}(t^*) = 0 \Rightarrow \dot{\vec{x}}(t^*) = 0$ $\Rightarrow \vec{x}(t^*) = (0,0,1)$, and $\vec{x}(t) = (0,0,1)$ being a stationary point, but especially $x_k \geq 0$.
IN THE SECOND CASE we restrict ourselves to $x_1(t^*) = 0$ and $x_2(t^*), x_3(t^*) > 0$, because of the first case. From the minimality of t^*, we have that $\dot{x_1}(t^*) < 0$. From the ODE (5) we have than the contradicition, that $\dot{x_1}(t^*) = 0 + P_{21}x_2(t^*) \geq 0$. This finishes the proof.
Beyond this it is shown that either $0 < x_i(t) < 1$ or that there is a stationary point $\vec{x} = \vec{e_i}$ for a unit vector $\vec{e_i} \in \mathbb{R}^3$. Similarly, one may show that for $P_{ij} > 0, x_i(0) > 0$ it follows, that

$$x_i(t) \in [0,1) \; \forall t \geq 0; \; i = 1,2,3.$$

2.4 The second Model

In a recent series of papers Müller et al. (cf. [2] and references there) have shown that from a thermodynamic point of view the coherency energy between (A, M) or (M^-, M^+) phases must be taken into account. Otherwise, there is no reason for the material, not to act as a fluid. Then, there would be no hysteretic behaviour. Müller shows, that the size of a hysteresis loop is dependent from
Müller chooses the simplest possible case with a value of $\sim A(1-A) = x_2(1-x_2)$, whose derivative appears with the proportionality factor ϵ for the coherency energy in the "new" transition probabilities as follows:

$$\begin{aligned} p^{-0} &= \tilde{C}_1 \cdot \frac{1}{\sqrt{\theta}} \cdot \exp\left(-\frac{f_1(P_E(t)) - 2\epsilon x_2}{\theta}\right) \\ p^{0-} &= C_1 \cdot \frac{1}{\sqrt{\theta}} \cdot \exp\left(-\frac{\tilde{f}_1(P_E(t)) + 2\epsilon x_2}{\theta}\right) \\ p^{+0} &= \tilde{C}_1 \cdot \frac{1}{\sqrt{\theta}} \cdot \exp\left(-\frac{f_2(P_E(t)) - 2\epsilon x_2}{\theta}\right) \end{aligned} \tag{7}$$

$$p^{0+} = C_1 \cdot \frac{1}{\sqrt{\theta}} \cdot \exp\left(-\frac{\tilde{f}_2(P_E(t)) + 2\epsilon x_2}{\theta}\right)$$

Here is the list of used abbreviations:

- p transistion probabilities, e.g., p^{0+} for the transition from austenite (whose phase fraction is x_2) to martensite+ (whose phase fraction is x_3);
- θ : the dimensionless absolute temperature;
- κ the ratio of curvatures K_A/K_M of the two parabola, by which the potential φ (cf. fig. 4) is constructed in this case;
- $\phi := \frac{\varphi(\mu_R)}{4K_M\mu_R^2}$;
- τ_X relaxation time of the phase fractions;
- τ_T relaxation time of the temperature;
- $C_1 := R/\tau_X\sqrt{1-\kappa/(4\phi)}$, $\tilde{C}_1 := C_1/\sqrt{\kappa}$;
- $f_{1,2} := \phi \cdot P_E^2 \pm K_1 \cdot P_E + K_2$;
- $\tilde{f}_{1,2} := \phi/\kappa \cdot P_E^2 \pm P_E + K_3$, where
- $K_1 := 1 - 1/\delta$, $K_2 := 1 + \epsilon$, $K_3 := \kappa/(4\phi) - \epsilon$;
- $\delta = \mu_R/J$, where J is the abscissa, where φ is in its lateral minimum (cf. fig. 4).

With the abbreviation

$$F_{1,3} := \left(1 - \frac{1}{\kappa}\right) \cdot \phi \cdot P_E^2 \mp \frac{1}{\delta} \cdot P_E + \left(1 - \frac{1}{4}\frac{\kappa}{\phi}\right)$$

we arrive at the system for a soft loading device

$$\begin{aligned}
\dot{x}_1 &= -p^{-0}x_1 + p^{0-}x_2 \\
\dot{x}_2 &= p^{-0}x_1 - (p^{0-}x_2 + p^{0+})\,x_2 + p^{+0}x_3 \qquad (8)\\
\dot{x}_3 &= p^{0+}x_2 - p^{+0}x_3
\end{aligned}$$

$$\begin{aligned}
\dot{\theta} &= -\frac{1}{\tau_T}(\theta - \theta_E) + \frac{1}{\zeta}\left[F_1 \cdot \dot{x}_1 + F_3 \cdot \dot{x}_3\right] \qquad (9)\\
&\quad -\frac{\epsilon}{\zeta}\left[1 - 2x_2\right] \cdot \dot{x}_2
\end{aligned}$$

$$d(t) = (\kappa \cdot x_1 + x_2 + \kappa \cdot x_3) \cdot 2\frac{\phi}{\kappa}\delta \cdot P_E(t) - (x_1 - x_2) \qquad (10)$$

with some constant ζ. Notice that for given $P_E(t)$ and $\theta_E(t)$ we may compute $\vec{x}$ and θ. The corresponding deformation follows then from a purely algebraic relation (10).
We continue with studying some mathematical properties. The structure of the system is similar to the one of the first model. However, after bringing the derivatives of the system onto the left side, the resulting matrix B is regular, and so we have global existence, if the right-hand side is suitable.
Lemma 2 holds, of course, in this case, too. The following lemma guarantees that the transition probabilities in spite of the term $\frac{1}{\sqrt{\theta}}$ are well defined, at least for the case, when there is no loading, e.g., by simulating a temperature-induced phase transition.

Lemma 3 *Let $P_E \equiv 0$, $\theta \geq c_E \; \forall t \in [0,T]$ with a positive constant c_E and for the coefficient of the coherency energy, let $\epsilon < \min\{1, \frac{r}{4}\}$ with $r := \frac{\phi}{\kappa}$.*
Then there exists $c > 0$ with $\theta(t) \geq c \; \forall t \in [0,T]$.

Proof Let p_{ij} be the transition probabilities from (7). Then we have for them

$$f_{1,2} - 2\epsilon x_2 = K_2 - 2\epsilon x_2 \in [1-\epsilon, 1+3\epsilon] \Rightarrow f_{1,2} - 2\epsilon x_2 > 0$$

$$\tilde{f}_{1,2} + 2\epsilon x_2 = \frac{1}{4r} - \epsilon + 2\epsilon x_2 \in \frac{1}{4r} + [-\epsilon, \epsilon] \Rightarrow \tilde{f}_{1,2} + 2\epsilon x_2 > 0$$

$$\Rightarrow \lim_{\theta \to 0} p_{ij}(\theta) = \lim_{y \to \infty} \frac{\exp(-Ky)}{y^{-\frac{1}{2}}} = 0$$

with a positive constant K. Assume that there is a monotone increasing sequence t_n with $\lim_{n\to\infty} \theta(t_n) = 0$.
After a possible change to a subsequence t_{n_i}, we can assume

$$\lim_{i\to\infty} \theta_i = 0 \text{ and } \lim_{i\to\infty} \dot{\theta}_i \leq 0$$

with $\theta_i := \theta(t_{n_i})$ and $\dot{\theta}_i$ analogously. The evolution of the phase fractions is due to (8) stationary: $\lim_{i\to\infty} \dot{x}_k(t_{n_i}) = 0$ $(k = 1,2,3)$. For $E_i := \left[\sum_{k=1,3} (F_k \dot{x}_k) - \epsilon(1-2x_2)\dot{x}_2\right]_{t_{n_i}}$ we have therefore due to $F_{1,3}(P_E \equiv 0) = \text{const.}$: $\lim_{i\to\infty} E_i = 0$, i.e. $\lim_{i\to\infty} E_i - \frac{\theta_i}{\tau_T} = 0$.
Due to $c_E > 0$ we find by applying (9) for every $\tilde{\epsilon} > 0$ a $N \in \mathbb{N}$ with

$$\dot{\theta}_i = \frac{\theta_E(t_{n_i})}{\tau_T} + \underbrace{\left(E_i - \frac{\theta_i}{\tau_T}\right)}_{|\cdot| \leq \tilde{\epsilon}} \geq \frac{c_E}{\tau_T} - \tilde{\epsilon} > 0 \; \forall i \geq N; \;\; \text{if e.g. } \tilde{\epsilon} < \frac{c_E}{\tau_T}$$

From this and the assumption about $\dot{\theta}_i$, for i sufficiently large, follows the contradiction

$$0 \geq \dot{\theta}_i > 0.$$

□

Lemma 4 *For P_E, $\theta_E \in L^\infty(0,T)$ there is a constant $C > 0$, such that $\theta(t) < C \; \forall t \in [0,T]$.*

Proof Assume t_n being a monotone increasing sequence with $\theta(t_n) \to +\infty$. Obviously $f_{1,2}, \tilde{f}_{1,2} \in L^\infty[0,T]$, because $x_2 \in [0,1]$, due to lemma 2. So $p_{ij}(t_n) \sim \frac{\exp(-K\theta(t_n))}{\sqrt{\theta(t_n)}} \overset{n\to\infty}{\longrightarrow} 0$. Inserting this into (8) we observe for $E_1 := \sum_{k=1,3} F_k \dot{x}_k \to 0$ and $E_2 := -(1-2x_2)\dot{x}_2 \to 0$, because $P_E, \theta_E \in L^\infty(0,T)$. By testing (9) with θ, integrating over $[0,T]$ and using Young's inequality, we arrive at

$$\begin{aligned}
\frac{1}{2}\,\theta^2\big|_0^T + \int_0^T \theta^2 dt &= \frac{1}{\tau_T}\int_0^T (\theta_E + E_1 + E_2)\cdot\theta dt \\
&\leq \frac{1}{\tau_T}\left(\delta^2 \int_0^T \theta^2 dt + \int_0^T [\theta_E + E_1 + E_2]^2\, dt\right) \\
\Rightarrow \frac{1}{2}\,\theta^2\big|_0^T + C_1 \int_0^T \theta^2 dt &\leq \int_0^T [\theta_E + E_1 + E_2]^2\, dt \leq C_2
\end{aligned}$$

with suitable constants $C_1, C_2 > 0$, which finishes the proof. □

For both models, it is easy to make the necessary changes from a model for a soft loading device to one for a hard loading device.

3 Numerical Simulations vs. Measurements from Experiments

Let us start with a soft loading device and the first model.
Remember, that matrix B of the system (3) may become singular, because we were not successful in excluding this by analytical means (e.g. a priori estimates). So

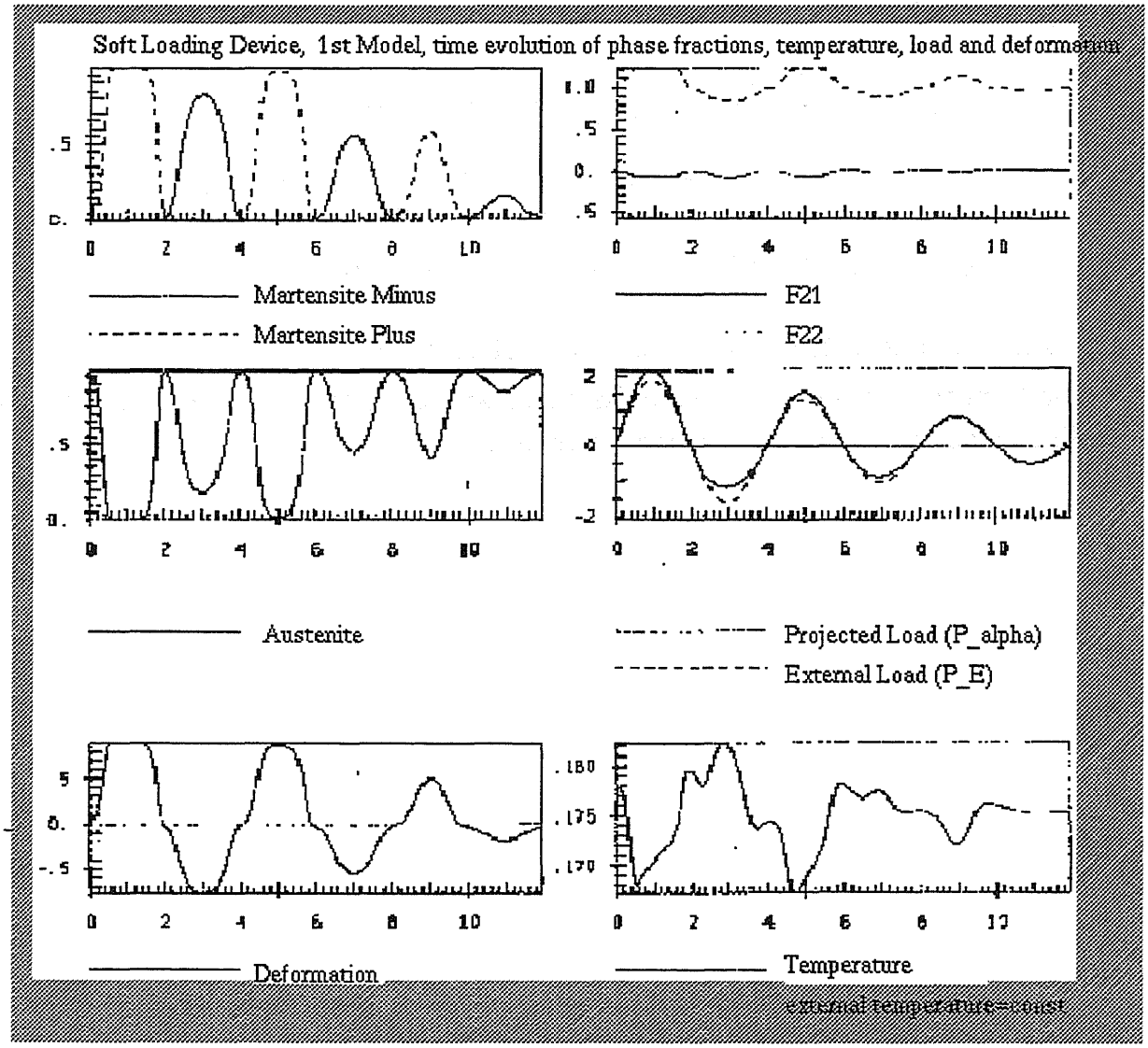

Fig. 5: Simulation soft loading device: left: phase fractions and deformation vs. time, right: F_{21}, F_{22}, external load P_E,τ_α and temperature vs. time

we have chosen a BDF-solver for DAEs (LSODI) instead of ODEs. To simplify the scheme, we transformed system (2) into the modified system

$$M\,\dot{Y} = F(t, Y)$$

with

$$M := \begin{pmatrix} I & 0 \\ 0 & 0 \end{pmatrix}, Y := \begin{pmatrix} y \\ z \end{pmatrix} \text{ and}$$

$$F(t,Y) := \begin{pmatrix} z \\ B(y) \cdot z - f(t,y) \end{pmatrix}.$$

So the left-hand side of the modified problems consists only of the singular matrix M, which is now constant. The whole system is packed into the right-hand side F. To compute therein B and f, it is necessary to evaluate the (partially semiinfinite) integrals (6), which is done to some extent by numerical approximations via Gauss-Hermite resp. Laguerre formula resp. by analysis. However, the dimension of the resulting system has doubled now.

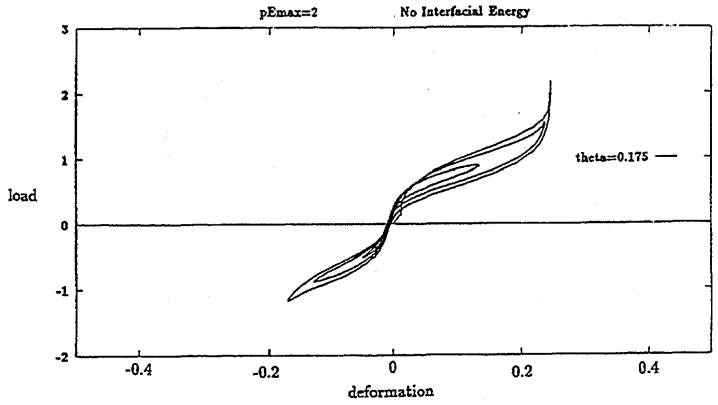

Fig. 6: Simulated load-deformation diagram for given external load, which is fading away.

In the second picture of the right-hand side of fig. 5 we see the given evolution of P_E and the resulting force on the layers τ_α (here denoted `P_alpha`), which are different, because during the simulation, the angle α of the layers is changing. At the bottom of the right-hand side, we can observe slight changes in temperature, due to the effects of *latent heat* during the transitions.
The left-hand side describes the development of the phase fractions (first subfigure martensite M^- and M^+, second one for austenite A) and the last subfigure shows the computed deformation for the given load.
In fig. 6 the resulting load-deformation diagram shows a asymmetry between the first and third quadrant, which is due to the fact, that during the hysteresis loop, the angle α and therefor also the load τ_α is changing.

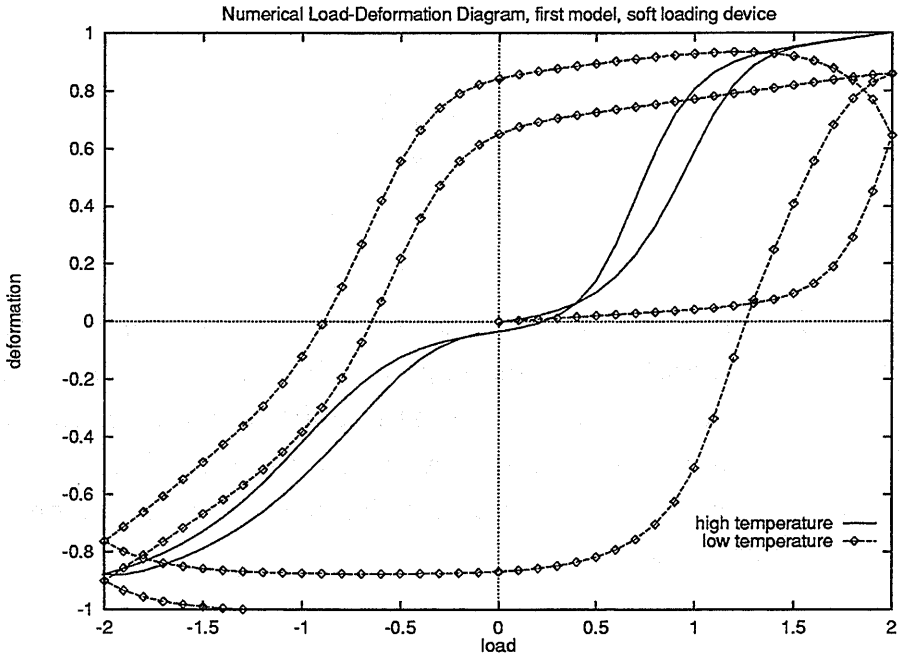

Fig. 7: Simulated load-deformation diagram 1st model for 2 different temperatures/soft loading device

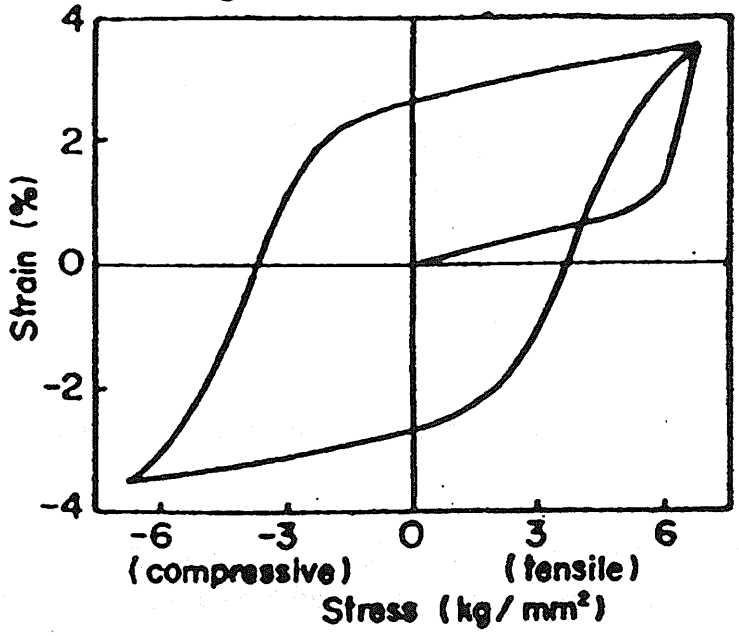

Fig. 8: Measured load-deformation diagram (ref. fig. 18 in [9])

Now we consider, still for the case of a soft loading device and the first model, a saw-toothed external load $P_E(t)$.

The numerical results (fig. 7) for this setting show a good qualitative agreement with experimental data of Murakami [9] in fig. 8. Notice that the shape memory effect as described in section 1.1 can be read of in fig. 7, where the dotted curve describes the load-deformation cycle at a low temperature with residual deforma-

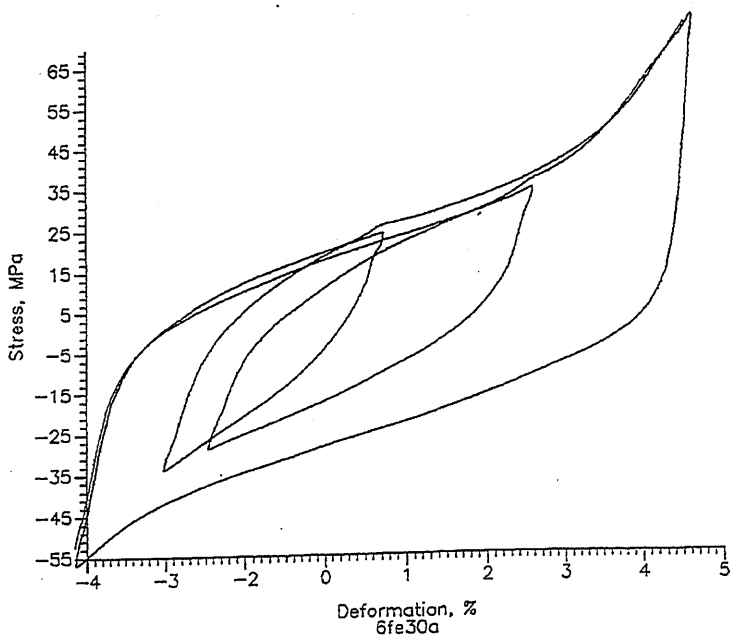

Fig. 9: Measured load-deformation diagram (in courtesy of U. Glasauer, TU-Berlin, cf. [10])

tions. After heating, the continuous curve applies, showing a zero deformation for zero external loads. We have not calculated the corresponding diagrams of the second model in the case of a soft loading device.
In fig. 9-11 we compare the experimental load-deformation diagrams with the numerical results for the case of a hard loading device. The programs are built in analogy to those for the first model. However, the physcial constants of [?? and private communication with I. Müller] are used.
By simulation a hard loading device, we can reproduce "inner loops" (cf. [8]) for both models (fig. 10-11). Comparing the simulations with experimental data (fig. 9), the second model (with *coherency energy*) shows its superiority to the first one, because in fig. 10, the "inner loops" have intersections with the outer one. So, the first model would predict thermodynamically unrealistic crosspoints in the loops. The simulations, done by the second model, have these artefacts not and the loops are much smoother, compared to the experiment.

3.1 Summary

We have discussed the Shape Memory Effect and pointed out, how it may be visualized by load-deformation diagrams for different temperatures. Using two models of I. Müller et al., based on statistical mechanics, we presented numerical simulations of load-deformation diagrams. In the setting of a soft loading device the first

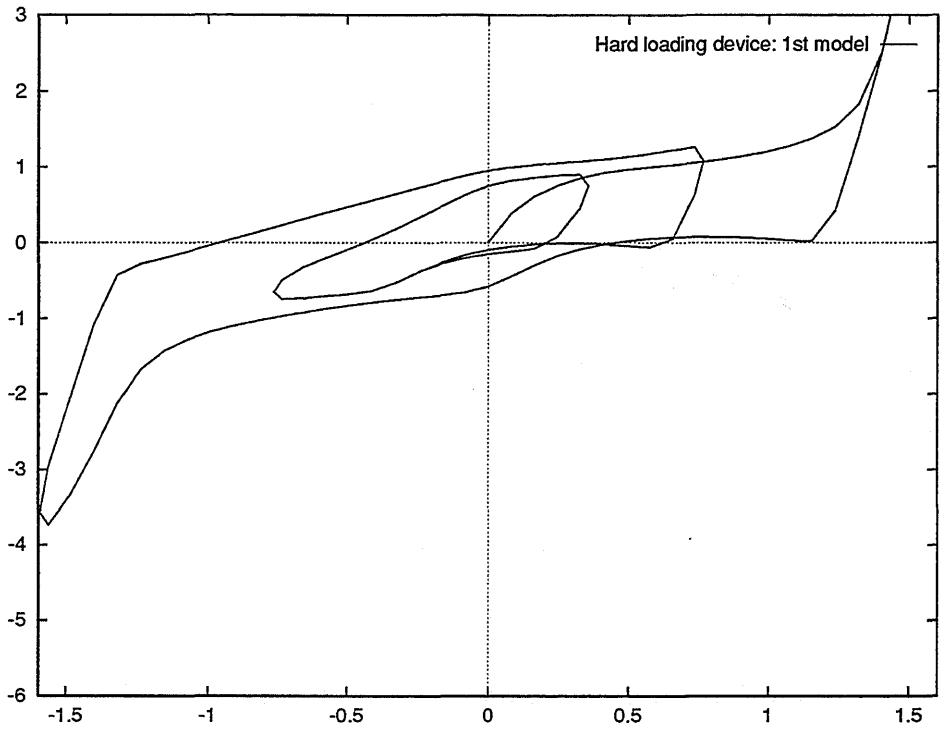

Fig. 10: Simulation hard loading device: 1st model

model shows a good qualitative agreement with experimental data. But in the case of a hard loading device then 2nd model can be seen as superior, especially when we simulate "inner loops", which can only be observed in this sort of experiments. It remains to confirm that the 2nd model can reproduce the *internal recovery line* (ref. [3]) in the quasiplastic- and pseudoelastic temperature range.

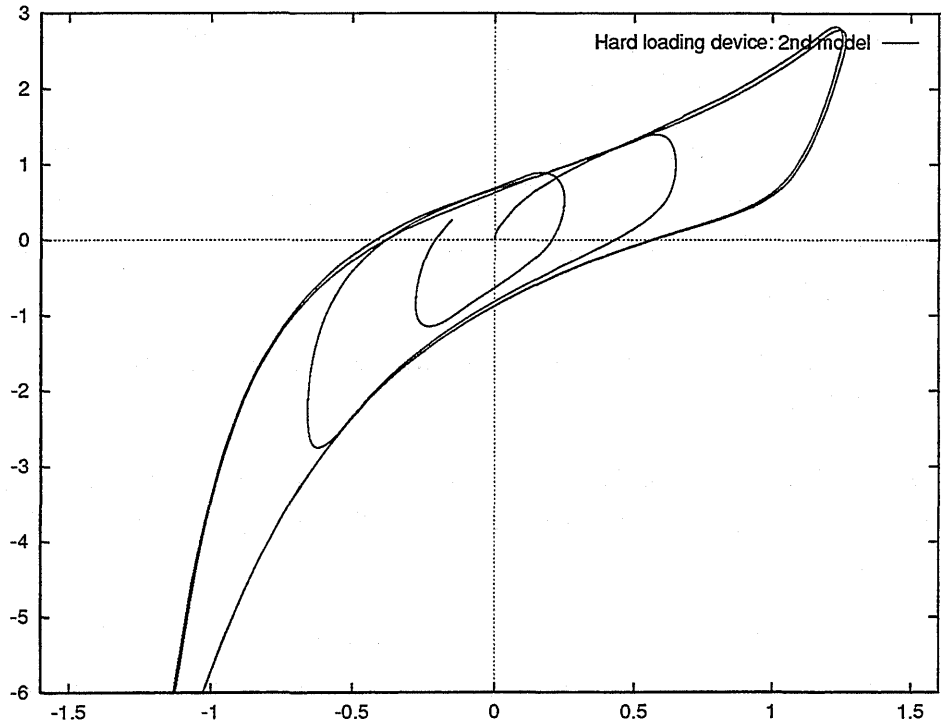

Fig. 11: Simulation hard loading device: 2nd model

4 Acknowledgement

The grant of DFG (Deutsche Forschungsgemeinschaft) within the frame work of the project SPP "Anwendungsorientierte Optimierung und Steuerung" for a part of this research is gratefully appreciated.

References

[1] ACHENBACH M., ATANACKOVIC T., MÜLLER I.: A Model for Memory Alloys in Plane Strain; Int. J. Solids Structures Vol. 22, No. **2** (1986), 171-193

[2] HUO Y.-Z., MÜLLER I.: Nonequilibrium Thermodynamics of Pseudoelasticity; Continuum Mech. Thermodyn. **5** (1993), 163-204

[3] HUO Y.-Z., MÜLLER I., SEELECKE ST.: Quasiplasticity and Pseudoelasticity in Shape Memory Alloys; in Phase Transitions and Hysteresis, Montecatini Terme 1993 (ed. A. VISINTIN), Springer Lecture Notes in Mathematics 1584, Berlin Heidelberg (1994)

[4] FALK, F.: One-dimensional model of shape memory aloys; Archive of Mechanics **35** (1983), 63-84

[5] SPREKELS J., ZHENG S.: Global Solutions to the Equations of a Ginzburg Landau Theory for structural Phase Transitions in Shape Memory Alloys: Physica D **39** (1989), 59-76

[6] NIEZGODKA M., SPREKELS J.: Convergent numerical approximations of the thermomechanical phase transitions in shape memory alloys: Numerische Mathematik **58** (1991), 759-778

[7] KLEIN O.: Stability and Uniqueness Results for a Numerical Approximation of the Thermomechanical Phase Transitions in Shape Memory Alloys, Advances in Mathematical Sciences And Applications **5** (1995), 91-116.

[8] BUBNER N.: Modellierung dehnungsgesteuerter Phasenübergänge in Formgedächtnislegierungen; Dissertation Universität GH Essen (1995), Shaker Verlag Aachen

[9] MURAKAMI Y.: Lattice Softening, Phase Stability and Elastic Anomaly of the β-Au-Cu-Zn alloy, J. of the Phys. Soc. of Japan, Vol. 33, **5** (1972)

[10] GLASAUER U.: Dissertation TU Berlin (1996), in preparation.

Recent publications of the Weierstraß–Institut für Angewandte Analysis und Stochastik

Preprints 1996

222. Jürgen Sprekels, Dan Tiba: A duality–type method for the design of beams.

223. Wolfgang Dahmen, Bernd Kleemann, Siegfried Prößdorf, Reinhold Schneider: Multiscale methods for the solution of the Helmholtz and Laplace equation.

224. Herbert Gajewski, Annegret Glitzky, Jens Griepentrog, Rolf Hünlich, Hans–Christoph Kaiser, Joachim Rehberg, Holger Stephan, Wilfried Röpke, Hans Wenzel: Modellierung und Simulation von Bauelementen der Nano– und Optoelektronik.

225. Andreas Rathsfeld: A wavelet algorithm for the boundary element solution of a geodetic boundary value problem.

226. Sergej Rjasanow, Wolfgang Wagner: Numerical study of a stochastic weighted particle method for a model kinetic equation.

227. Alexander A. Gushchin: On an information–type inequality for the Hellinger process.

228. Dietmar Horn: Entwicklung einer Schnittstelle für einen DAE–Solver in der chemischen Verfahrenstechnik.

229. Oleg V. Lepski, Vladimir G. Spokoiny: Optimal pointwise adaptive methods in nonparametric estimation.

230. Bernd Kleemann, Andreas Rathsfeld, Reinhold Schneider: Multiscale methods for boundary integral equations and their application to boundary value problems in scattering theory and geodesy.

231. Jürgen Borchardt, Ludger Bruell, Friedrich Grund, Dietmar Horn, Frank Hubbuch, Tino Michael, Horst Sandmann, Robert Zeller: Numerische Lösung großer strukturierter DAE–Systeme der chemischen Prozeßsimulation.

232. Herbert Gajewski, Klaus Zacharias: Global behaviour of a reaction–diffusion system modelling chemotaxis.

233. Fréderic Guyard, Reiner Lauterbach: Forced symmetry breaking perturbations for periodic solutions.

234. Vladimir G. Spokoiny: Adaptive and spatially adaptive testing of a nonparametric hypothesis.

235. Georg Hebermehl, Rainer Schlundt, Horst Zscheile, Wolfgang Heinrich: Simulation of monolithic microwave integrated circuits.

236. Georg Hebermehl, Rainer Schlundt, Horst Zscheile, Wolfgang Heinrich: Improved numerical solutions for the simulation of monolithic microwave integrated circuits.

237. Pavel Krejčí, Jürgen Sprekels: Global solutions to a coupled parabolic–hyperbolic system with hysteresis in 1–d magnetoelasticity.

238. Georg Hebermehl, Friedrich–Karl Hübner: Portabilität und Adaption von Software der linearen Algebra für Distributed Memory Systeme.

239. Michael H. Neumann: Multivariate wavelet thresholding: a remedy against the curse of dimensionality?

240. Anton Bovier, Miloš Zahradník: The low–temperature phase of Kac–Ising models.

241. Klaus Zacharias: A special system of reaction equations.

242. Susumu Okada, Siegfried Prößdorf: On the solution of the generalized airfoil equation.

243. Alexey K. Lopatin: Oscillations and dynamical systems: Normalization procedures and averaging.

244. Grigori N. Milstein: Stability index for invariant manifolds of stochastic systems.

245. Luis Barreira, Yakov Pesin, Jörg Schmeling: Dimension ofhyperbolic measures – A proof of the Eckmann–Ruelle conjecture.

246. Leonid M. Fridman, Rainer J. Rumpel: On the asymptotic analysis of singularly perturbed systems with sliding mode.

247. Björn Sandstede: Instability of localised buckling modes in a one–dimensional strut model.

248. Björn Sandstede, Christopher K.R.T. Jones, James C. Alexander: Existence and stability of N–pulses on optical fibers with phase–sensitive amplifiers.

249. Vladimir Maz'ya, Gunther Schmidt: Approximate wavelets and the approximation of pseudodifferential operators.

250. Gottfried Bruckner, Sybille Handrock–Meyer, Hartmut Langmach: On the identification of soil transmissivity from measurements of the groundwater level.